AGU PUBLICATIONS

JGR

Journal of Geophysical Research: Solid Earth

RESEARCH ARTICLE
10.1002/2014JB011051

Key Points:
- Elastic wave speed and amplitude vary systematically during the seismic cycle
- Porosity and shear fabric influence fault zone elastic wave speeds
- Sound velocity provides an important proxy for fault strength evolution

Correspondence to:
B. M. Kaproth,
bkaproth@gmail.com

Citation:
Kaproth, B. M., and C. Marone (2014), Evolution of elastic wave speed during shear-induced damage and healing within laboratory fault zones, *J. Geophys. Res. Solid Earth*, *119*, 4821–4840, doi:10.1002/2014JB011051.

Received 18 FEB 2014
Accepted 3 MAY 2014
Accepted article online 8 MAY 2014
Published online 3 JUN 2014

Evolution of elastic wave speed during shear-induced damage and healing within laboratory fault zones

Bryan M. Kaproth[1] and Chris Marone[1]

[1]Department of Geosciences, Pennsylvania State University, University Park, Pennsylvania, USA

Abstract Earthquake faults fail and restrengthen repeatedly during the seismic cycle. Faults restrengthen via a set of processes known collectively as fault healing, which is well documented in the laboratory but less well understood in tectonic fault zones. Recent observations of fault zone wave speed following earthquakes suggest opportunities to connect laboratory and field observations of fault healing. However, existing laboratory data lack detail necessary to identify specific processes linking elastic wave speed to fault damage and healing. Here we document changes in elastic properties during laboratory seismic cycles, simulated via periods of nonshear and quasistatic fault slip. Experiments were conducted on brine-saturated halite under conditions favoring pressure solution, analogous to healing processes within and at the base of the seismogenic zone. We find that elastic wave speed (V) and amplitude (A) correlate with porosity. For each percent of porosity lost during compaction, V_P increases by ~3%, V_S by ~2%, A_P by ~10%, and A_S by ~7%. Moreover, V and A decrease with granular dilation during fault slip. With increasing shear strain, fabric formation dominates the ultrasonic signals. We find that fault strength depends on fault porosity, making V_P and V_S potential proxies for fault strength evolution. Our data show that a 1% change in V_P or V_S results in a friction increase of 0.01 or 0.02, respectively. Within natural fault zones, advances in monitoring elastic wave speed may provide critical information on the evolution of fault strength and seismic hazard throughout the seismic cycle.

1. Introduction

Earthquakes have long been understood as dynamic frictional failure events along fault zones. Failure initiates when tectonic stresses exceed the fault strength, releasing elastic strain energy seismically and through damage to the fault zone. Following rupture, fault zones heal and tend to regain strength with the logarithm of time [*Scholz*, 2002]. During this interseismic period, tectonic strain slowly rebuilds and accumulates elastic strain energy until the next rupture [*Brace and Byerlee*, 1966].

Recent studies have illuminated earthquake damage and recovery in areas surrounding faults. These studies focus on spatiotemporal changes in elastic wave speed through the seismic cycle and typically show coseismic velocity decrease and subsequent recovery with log time [Baisch and Bokelmann, 2001; *Vidale and Li*, 2003; *Rubinstein and Beroza*, 2004; *Schaff and Beroza*, 2004; *Li et al*., 2006; *Chao and Peng*, 2009; *Sawazaki et al*. 2009; *Nakata and Snieder*, 2011; *Minato et al*., 2012; *Schaff*, 2012; *Takagi et al*., 2012; *Liu et al*., 2013; *Xue et al*., 2013]. While these data cannot provide estimates of fault strength evolution, owing to their off-fault focus, they do provide insight on the extent of in situ earthquake damage and the processes of fault healing and damage recovery.

Elastic wave speed changes have been observed for earthquakes including the 1979 M 5.9 Coyote Lake [*Poupinet et al*., 1984], 1999 M 7.1 Hector Mine [*Li et al*., 2003], 1992 M 7.3 Landers [*Li et al*., 1998; *Li and Vidale*, 2001; *Vidale and Li*, 2003], 1984 M 6.2 Morgan Hill [*Schaff and Beroza*, 2004], 2000 Western Tottori [*Sawazaki et al*., 2009], 2004 M 6.6 mid-Niigata [*Wegler and Sens-Schoenfelder*, 2007], 2004 M 6 Parkfield [*Rubinstein and Beroza*, 2005; *Li et al*., 2006], 2008 Iwate-Miyagi Nairiku [*Yamada et al*., 2010], 2008 M 7.9 Wenchuan [*Liu et al*., 2013], and the 2011 M 9 Tohoku-Oki [*Nakata and Snieder*, 2011; *Nakata and Snieder*, 2012] events. These studies used a variety of sources including repeating earthquakes [e.g., *Rubinstein and Beroza*, 2005], chemical explosions [e.g., *Li et al*., 1998], and the rapidly advancing field of ambient seismology [e.g., *Nakata and Snieder*, 2011] to image changes in elastic wave speed in the fault zone region. *Li et al*. [2006] used fault zone guided waves to study fault healing, and they were able to provide the tightest spatial resolution around the fault zone to date, ~200 m. These damage zone observations

showed ~2.5% *S* wave velocity decrease after the 2004 *M* 6.0 Parkfield earthquake, followed by ~1% recovery over 3 months.

Changes in elastic wave speed in areas surrounding active faults are thought to occur by processes of crack opening and healing, driven by the seismic cycle and modulated by regional stresses and fluid migration [*Li et al*., 1998, 2003, 2006; *Vidale and Li*, 2003; *Silver et al*., 2007; *Niu et al*., 2008; *Schaff*, 2012]. Similarly, it has been suggested that permeability of country rock may also experience coseismic increase and subsequent healing [*Elkhoury et al*., 2006]. Damage within the fault zone likely occurs by processes of dilation, compaction, cracking, shear driven comminution, and fabric generation. While these changes tend to be difficult to observe in nature, owing to the narrow width of many active fault zones [*Faulkner et al*., 2010], recent advances in borehole instrumentation near fault zones (e.g., San Andreas Fault Observatory at Depth (SAFOD)) [*Niu et al*., 2008] may offer tighter spatial resolution in the future.

Elastic wave properties within fault zones are likely to be strongly influenced by porosity evolution through the seismic cycle. The effective elastic moduli, and thus V_P and V_S, of a granular zone are controlled by grain coordination number, grain contact stiffness, and grain contact geometry, which are all affected by stress state and porosity, in addition to pore fluid and the composition of the grains themselves [*Digby*, 1981; *Makse et al*., 2004; *Khidas and Jia*, 2010, 2012; *Knuth et al*., 2013]. Previous experimental works have related porosity to elastic wave speed through compaction experiments on sediments and/or across suites of similar rocks at different compaction states [e.g., *Hadley*, 1976; *Popp and Kern*, 1998; *Schubnel et al*., 2003; *Fortin et al*., 2005, 2007; *Croizé et al*., 2010; *Kitajima and Saffer*, 2012; *Knuth et al*., 2013]. Elastic wave speeds tend to increase linearly with compaction in the range of typical rock porosities, $\phi < 30$–40% [*Erickson and Jarrard*, 1998; *Mavko et al*., 2009]. However, these works do not focus on repeated compaction and dilation in a given rock, which occurs within faults over the seismic cycle [*Mead*, 1925; *Faulkner et al*., 2010]. Thus, the role of hysteresis has not been established. Additionally, fault zones develop fabric and heterogeneities with shear [*Logan et al*., 1992, *Haines et al*., 2013], which may result in unexpected velocity effects relative to bulk ϕ [e.g., *Knuth et al*., 2013].

In this paper we discuss the evolution of elastic wave properties within a laboratory fault zone during analog seismic cycles, which consist of shear and nonshear periods. These experiments were carried out on granular halite under brine-saturated conditions, analogous to midcrustal rocks in the deep seismogenic zone, where frictional healing occurs largely via pressure solution. In general, we observe velocity reduction with fault slip and subsequent recovery with log time during "interseismic" periods. These data highlight a strong relationship between fault porosity and elastic properties during both shear and nonshear periods. At the laboratory scale, our observations suggest that ultrasonic observations may be a useful tool to infer porosity changes and fabric evolution. At the field scale, our observations suggest that elastic wave speed changes within fault zones and damage zones may be a proxy for bulk porosity changes and could provide critical information on fault zone strength evolution.

In the Methods section, we describe our experimental procedure, including the experimental geometry and materials used, and discuss specific methods and limitations for ultrasonic and porosity measurements. In the results section, we describe the frictional behavior of a fault during analog seismic cycles, the cyclic nature of porosity change through these periods, and the attendant response of ultrasonic velocities and amplitudes to porosity change. In the discussion and conclusion sections, we focus on the relationships between strength, porosity, and elastic properties throughout the seismic cycle. In particular, we highlight broad-scale compaction and dilation trends, subtle porosity changes, and the confounding aspect of fabric evolution, which may be useful for future laboratory studies. Finally, we tie our observations to recent field studies, which describe short- and long-term velocity evolution in response to earthquakes, and suggest that similar observations within active fault zones, perhaps using trapped waves, may provide a useful proxy to monitor in situ fault strength evolution.

2. Methods and Materials

Our experiments were conducted on ground halite in the biaxial forcing apparatus at Penn State. Figure 1 shows the double-direct shear geometry, which consists of two fault zones sandwiched between three steel blocks. For details, see *Anthony and Marone* [2005] and *Kaproth et al*. [2010]. Normal stress (σ_n) is

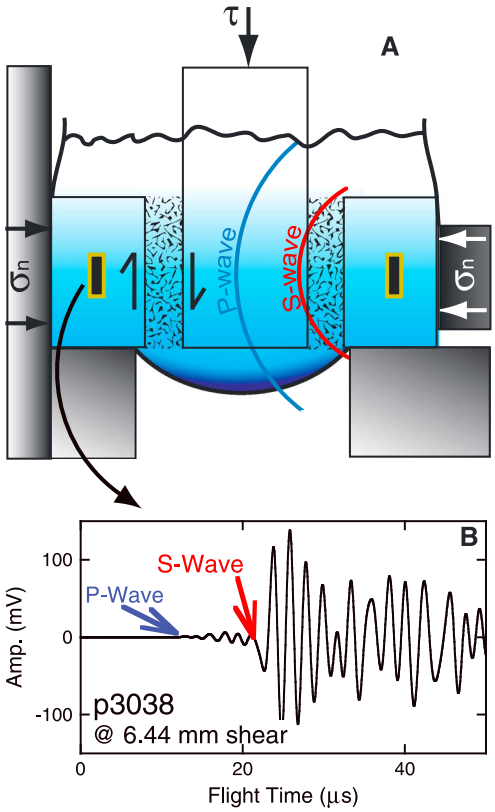

Figure 1. (a) Double-direct shear experiments were conducted under biaxial stress and were brine saturated. Ultrasonic velocities and amplitudes were continuously measured via *S* wave piezoelectric transducers (0.5 MHz). (b) An example stacked seismogram shows a large *S* wave with a small mode-converted *P* wave.

applied horizontally, and displacement is imposed at the center block, inducing shear within the fault gouge layers. Fast-acting servohydraulic controllers maintain specified horizontal load and vertical displacement rate. Strain gauge load cells accurate to ±0.1 kPa measured vertical and horizontal load. Direct current displacement transducers accurate to ±0.1 μm measured vertical and horizontal displacement (shear displacement and layer thickness, respectively). Stresses and displacements were recorded digitally at 10 kHz with a 24-bit system and were averaged to 10–100 Hz for storage.

Experiments were conducted on pure halite ground in a rotary mill and sieved to $<$125 μm. We constructed initial sample layers that were 0.5 cm thick and 5 cm × 5 cm nominal frictional contact area. Layers were loaded to 0.5 MPa σ_n and soaked in salt-saturated brine for 1 h, after which normal stress was increased to 15 MPa. Figure 2 shows the effect of this procedure on ϕ. Samples were sheared 10 mm following this initial load up. This "run-in" period promoted development of a steady state shear fabric within the gouge layers [e.g., *Marone*, 1998; *Kaproth et al*., 2010; *Niemeijer et al*., 2010]. After the run-in, shear was stopped for a period ranging from 1 to 3000 s, to simulate the interseismic period and fault zone healing, after which shear was resumed for 2 mm. See Table 1 for experiment details. In experiment p3636, we conducted multiple hold periods (1 to 3000 s), each followed by 2 mm of shear.

At the end of each experiment, shear stress was removed, the brine was drained, and the final sample thickness was measured. The samples were recovered intact from the side blocks after normal stress was removed. Once recovered, the samples were flushed with pure isobutyl alcohol, oven dried, and weighed.

2.1. Continuous Measurement of Elastic Wave Speed and Amplitude

Ultrasonic measurements were made throughout these experiments to investigate the possible relationship of elastic wave speeds with fault zone porosity, fault strength, and fault healing. These measurements were made via high-frequency sound waves, limiting sample disturbance [e.g., *Khidas and Jia*, 2010; *Johnson et al*., 2012; *Knuth et al*., 2013], and these observations were continuous, making any physical conditioning consistent across this entire data set. The following section describes the acoustic setup, details of wave processing and calibrations, and includes discussion of error and its sources.

Continuous ultrasonic measurements were made via two 0.5 diameter shear wave piezoelectric transducers (500 kHz, lead zirconate titanate) from Boston Piezo Optics (D31 piezoelectric lead zirconate titanate (PZT)-5a). The transducers were bonded to a well within the loading platens of the double-direct shear configuration (Figure 1). We excited one transducer with a 900 V pulse generated by an Olympus NDT model 5058PR pulser-receiver. At this voltage, an ~0.15 μm amplitude *S* wave is generated (0.171 nm/V piezoelectric constant). *P* waves are generated simultaneously by mode conversion, but their amplitude tended to be ~5% of the *S* waves. Elastic waves were received by an identical PZT transducer in the opposite side block (Figure 1). We measured elastic properties in five experiments (labeled "AC" in Table 1), and for consistency, all experiments were exposed to this continuous ultrasonic source. We recorded the

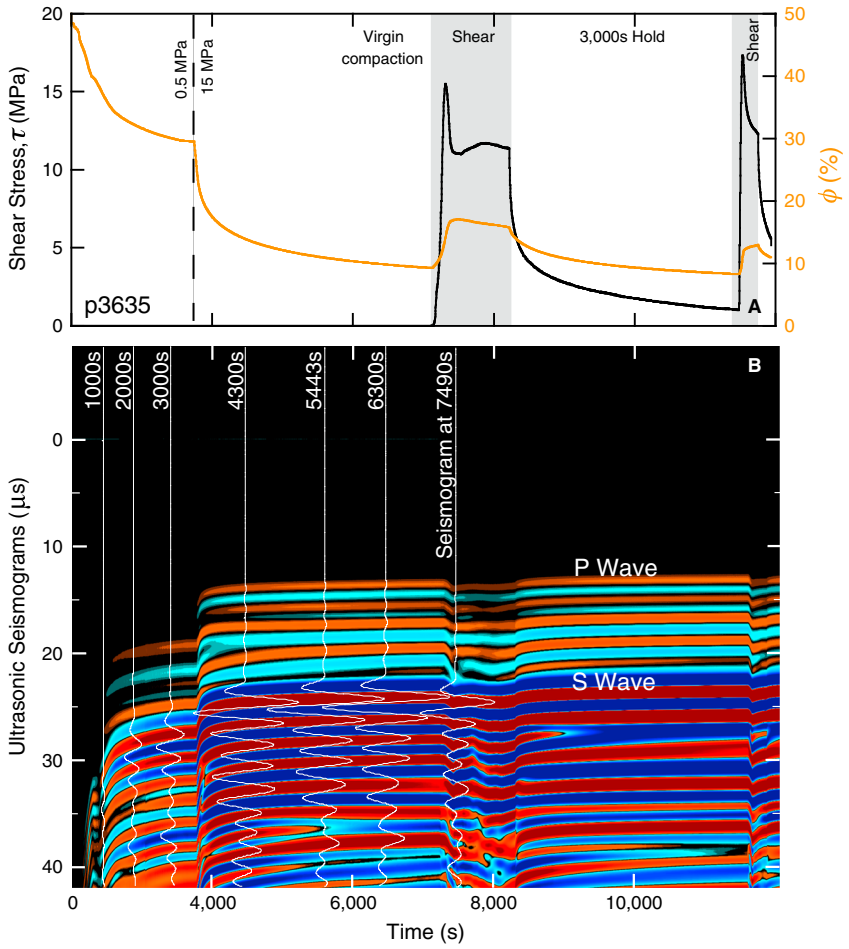

Figure 2. (a) Porosity evolution during an ~3 h experiment along with (b) attendant seismogram changes. Normal stress was held constant at 15 MPa, with initial compaction at 0.5 MPa. Porosity generally increases with shear and decreases during nonshear periods or "holds." Seismograms tend to change with porosity evolution.

Table 1. Experiment Details

Experiment	σ_n During Run-In (MPa)	σ_n Following Run-In (MPa)	Hold Time (s)	Shear Strain (γ)	Initial Mass (g)	Final Mass (g)	Measured Mass Loss (g)	Predicted Initial Mass (g)	Predicted Mass Loss (g)
p3635 AC	15	15	3,000	3.3	42.0	30.5	6.6	38.9	7.9
p3636 AC	15	15	1, 3, 10, 30, 300, and 3,000	7.3	42.4	25.2	16.1	40.1	14.0
p3453	15	15	10,000	5.0	33.2	22.9	7.3	32.4	7.9
p3456	15	15	10,000	4.5	36.1	24.0	7.9	35.7	8.7
p3457	15	15	30,000	4.6	36.4	26.4	7.3	35.5	8.6
p2977	30	15	3,000	8.7	25.5	17.4	7.3	24.9	7.0
p2984	30	15	30	9.1	25.0	16.7	6.7	23.9	6.7
p2986	30	15	none	9.4	23.0	16.0	5.7	23.0	6.5
p3020 AC	30	15	10,000	7.7	28.0	18.7	7.5	26.2	7.1
p3021 AC	30	15	none	5.9	25.9	19.9	5.1	25.6	5.3
p3022 AC	30	15	10,000	6.8	23.5	17.6	4.4	23.0	5.0
p3069	30	15	1,000	8.0	26.5	18.4	6.8	26.4	7.4
p3071	30	15	none	8.4	24.1	16.6	6.5	23.3	6.3
p3072	30	15	10,000	5.6	27.4	20.7	5.5	27.1	6.0
p3088	30	15	1,000	8.4	28.2	17.3	6.0	24.5	6.7

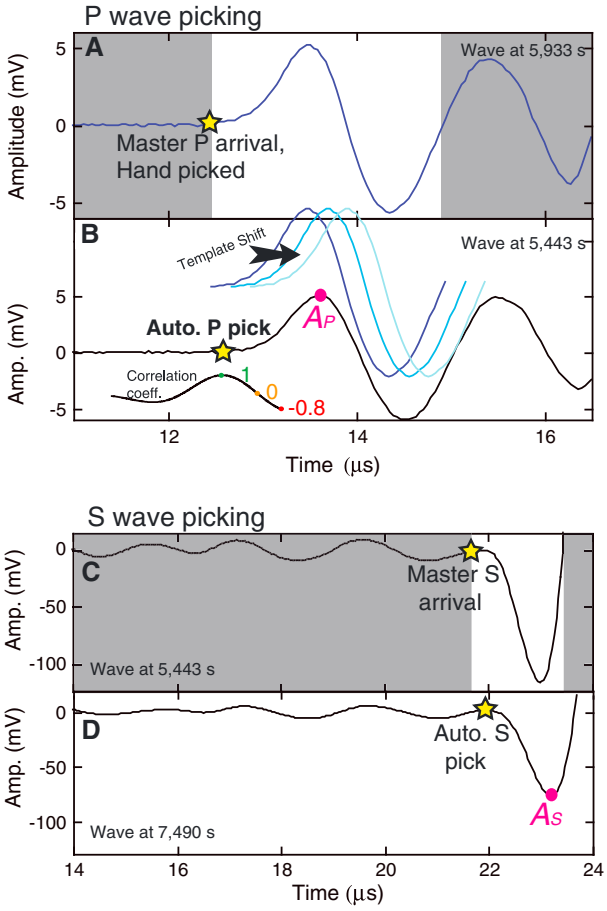

Figure 3. Example of *P* and *S* wave arrival picking via cross correlation. (a) Master *P* waves and (c) master *S* waves were selected for each experiment. (b and d) These waves were compared against each subsequent seismogram for best match, respectively. Amplitudes (A_P and A_s) were determined as the peak following arrival.

output response with a GaGe CS8382 multichannel digitizer at 25 MHz (14 bit). For most experiments, waveforms were stacked 100 per sample, and we record one waveform every 2 s (Figure 2b). We also recorded unstacked signals in some cases to provide higher temporal resolution. A typical experiment included 1000+ stacked waveforms (Figure 2b).

Our instrumentation was designed to optimize *P* and *S* wave arrival picking. With an *S* wave transducer, the *S* wave is very large compared to the *P* wave coda (Figure 3), making it relatively easy to pick. Additionally, the large excitation voltage made the *P* wave much larger than the background electronic noise. We built Faraday cages around each transducer to further isolate electronic noise.

We picked the *P* and *S* wave arrivals via cross correlation using standard seismic techniques [e.g., *Stein and Wysession*, 2003]. Cross correlation compares a master waveform to other seismograms, identifying a flight time shift. After selecting master waves with high signal-to-noise ratios (Figure 3a), we compared them against a moving window for every other seismogram in the experiment, making a pick at the highest correlation coefficient (Figure 3). In general, we found that cross correlation is most effective when the starting and ending points are near zero (<3% from 0). Figure 3b compares the *P* wave template to a seismogram from 500 s earlier. The template wave is compared against a moving window of the wave of interest. The pick is made at the maximum correlation coefficient (e.g., 12.6 μs; Figure 3b inset). One benefit of cross correlation is that it offers a 10X improvement in temporal resolution compared to the base sampling rate. Thus, we subsampled each master wave and seismogram with a 10X spline fit. Owing to the similarity of waveforms, maximum correlation coefficients are very high, generally >0.98 for *P* waves and >0.99 for *S* waves (Figure 4).

While using *S* wave transducers to generate simultaneous *P* and *S* waves offers distinct advantages (e.g., identical travel path and simple setup), it can make the *S* wave difficult to pick if it arrives in phase with the *P* coda. Our experiments included a simple solution to this problem. As the layer thins and velocities change, the *S* wave migrates through the *P* wave coda and eventually became out of phase (Figure 2). Because cross correlation only requires one master waveform, this master waveform was selected when the *S* wave is out of phase with the *P* coda.

We calculated the absolute *P* wave velocity throughout each experiment following

$$V_P = h/\left(T_P - T_P^0\right), \tag{1}$$

where h is the layer thickness, T_P is the *P* wave flight time, and $T^0{}_P$ is the *P* wave flight time from

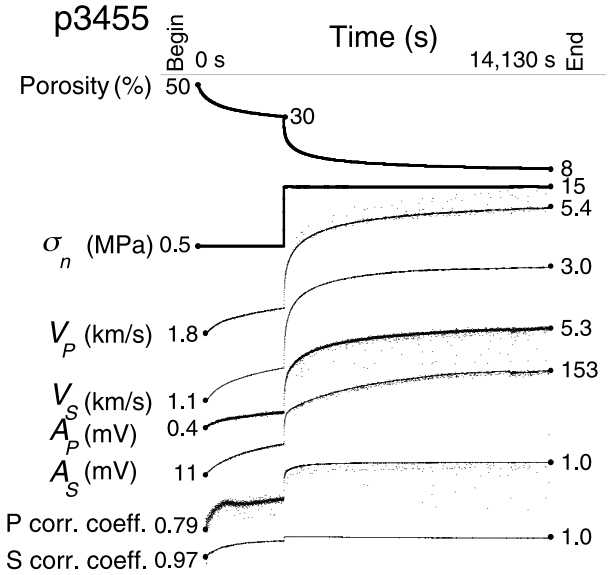

Figure 4. Experiment details under simple compaction. Compaction generally occurs with log time along with increases to the velocities and amplitudes. Correlation coefficients for *P* and *S* waves are generally high (>0.8) and become stronger with high amplitudes (>0.97).

calibrations with no gouge layer under similar normal loads. We similarly calculated the absolute *S* wave velocity following

$$V_S = h/\left(T_S - T_S^0\right), \tag{2}$$

where T_S is the *S* wave flight time and $T^0{}_S$ is the *S* wave flight time from calibrations. The calibrations were carried out repeatedly to verify results: $T^0{}_P = 11.1\ \mu s$ and $T^0{}_S = 19.1\ \mu s$.

We measured *P* and *S* wave amplitude (A_P and A_S) in these experiments at the peak following the first arrival (Figure 3). With a constant source and thin layer, thus limiting radial dispersion and attenuation, the dominant control on amplitude is the reflection coefficient, which is directly tied to impedance contrast between the sample and the forcing blocks [e.g., *Stein and Wysession*, 2003].

The two primary contributors to V_P and V_S measurements uncertainty are layer thickness and flight time. While changes in *h* were tracked precisely throughout each experiment, initial thickness was measured by hand with calipers to a precision of ±0.1 mm, contributing to absolute uncertainty. Additionally, forcing blocks in the double-direct shear configuration are subject to some tilting with shear strain, adding up to +0.15 mm of uncertainty. These contributions to measurement uncertainty impact the absolute accuracy of our wave speed estimates, but should not affect interpretation of short-term trends.

Uncertainty in the flight time measurement was ±0.08 μs, or <7% of the signal from p3635, and is derived from calibration uncertainty and the digital sampling rate. V_P and V_S error tended to be large at the end of the experiments, owing to layer thinning with strain and thus small values of *h*. Figure 5 shows absolute V_P and V_S uncertainties for p3635, which were, respectively, <~35% and <~10%. Our center V_P and V_S values are slightly greater than previously reported values for halite [*Lazarus*, 1949; *Mavko et al*., 2009], but fall in range when error is considered (Figure 5). Figure 6 compares our porosity-velocity trends (p3635) with the work of *Popp and Kern* [1998]. Although their work was on natural halite with some anhydrite and polyhalite, our trends are in general agreement.

Electronic noise was the primary contributor to A_P error, resulting in a cloud of data points (e.g., Figure 5). This noise did not affect the much larger *As* signal, but A_S was more sensitive to occasional power fluctuations, evident during the initial compaction in Figure 5. The major player for A_S error was convolution with the *P* wave coda. In general, the *P* wave coda was ~10% of the *S* wave amplitude (Figures 1, 3c, and 3d), adding up to ±10% error for A_S. However, this error is dependent on the gradually changing phase match (Figure 2). For example, in p3635, the *S* wave arrival was generally out of phase with the *P* wave coda (160–200°), limiting the relative error in p3635 to ±3.5%.

2.2. Continuous Porosity Measurements

Porosity is notoriously difficult to measure accurately and precisely in shear experiments. The root of this problem comes from difficulties in making accurate measurements of initial porosity under applied stresses and from mass loss during shear. The following section describes a new method to track mass loss, allowing for detailed, high-resolution porosity measurements.

We measured the absolute value of porosity at the beginning and end of each experiment, and we combined these values with precise measurements of layer thickness change to derive ϕ throughout each

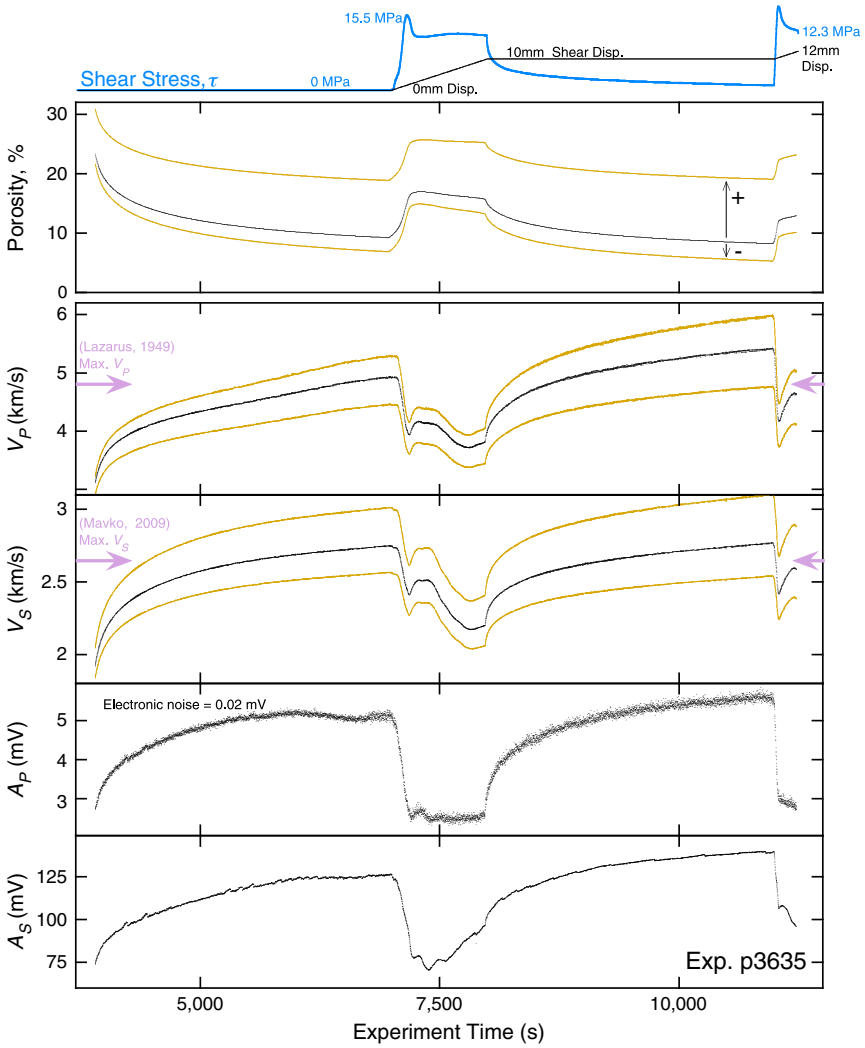

Figure 5. Porosity, velocity, and amplitude changes and uncertainty in an experiment with shear. Porosity decreased and V_P, V_S, A_P, and A_S increased during hold periods, similar to Figure 4, and these trends reversed during shear periods. Velocities and amplitudes typically relate inversely with ϕ changes.

experiment. At these endpoints, the sample mass (M), h, and contact area (A) are known. We calculate bulk density following

$$\rho_{\text{bulk}} = M/(h * A), \tag{3}$$

and porosity following

$$\varphi = 1 - (\rho_{\text{solids}} - \rho_{\text{bulk}})/\rho_{\text{solids}}, \tag{4}$$

where ρ_{solids} is the density of halite (2.16 g/cm^3). To calculate ϕ throughout each experiment, we account for h (which is measured continuously) and mass loss via geometric thinning [*Scott et al.*, 1994].

Geometric thinning is a phenomenon of mass shedding that occurs in any mode of simple or pure shear with the exception of ring shear under some boundary conditions [*Scott et al.*, 1994]. This mass loss must be accounted for to accurately determine ϕ throughout shearing. The standard model for geometric thinning is

$$h * \delta x * 0.5 = L * \delta h_{gt}, \tag{5}$$

where h is the layer thickness, δx is the instantaneous shear displacement, L is the sample length, and δh_{gt} is the incremental thickness change [*Scott et al.*, 1994]. This equation suggests that the mass is lost as a triangle

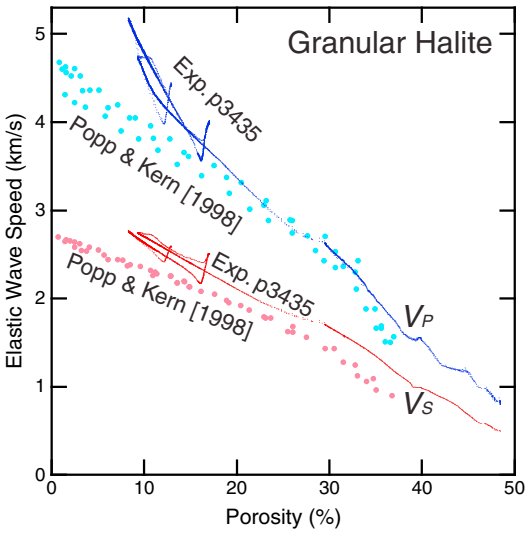

Figure 6. Ultrasonic velocities as a function of porosity for an entire experiment with shear and hold periods. V_P and V_S show an inverse linear relation with ϕ that remains consistent through compaction or dilation during hold and shear periods. Our results, shown here for p3635, compare favorably with the preexisting triaxial data set from *Popp and Kern* [1998], which was conducted on natural rock salt samples.

with shear, but alternate shapes are possible, especially considering the effects of localization and distributed shear [e.g., *Rathbun and Marone*, 2010]. In the interest of high-fidelity ϕ measurements, we calibrated the *Scott et al.* [1994] model for our experiments.

To calibrate the mass loss model, we measured mass loss as a function of shear offset in 14 experiments (Table 1). To estimate mass loss at any time during the experiment, we used a forward model with conservation of mass. Mass lost at a future time (t) can be estimated following

$$M^t_{\text{lost}} = \delta x^t * h^t * y * \rho^t_{\text{bulk}}, \tag{6}$$

where y is the width (5 cm) and δx is the incremental displacement. Therefore, sample mass and mass lost at any future time step can be predicted following

$$M^{t+1} = M^t - M^t_{\text{lost}}, \tag{7}$$

or alternatively:

$$\rho^{t+1}_{\text{bulk}} * h^{t+1} * x * y = \rho^t_{\text{bulk}} * h^t * x * y - \delta x^t * h^t * y * \rho^t_{\text{bulk}}. \tag{8}$$

There is uncertainty in density at the beginning of the experiment, owing to some mass extrusion when the sample is loaded. However, we have excellent mass constraint at the end of each experiment. Therefore, we run this model backward following

$$\rho^{t-1}_{\text{bulk}} * h^{t-1} * x * y = \rho^t_{\text{bulk}} * h^t * x * y + \delta x^t * h^t * y * \rho^t_{\text{bulk}}. \tag{9}$$

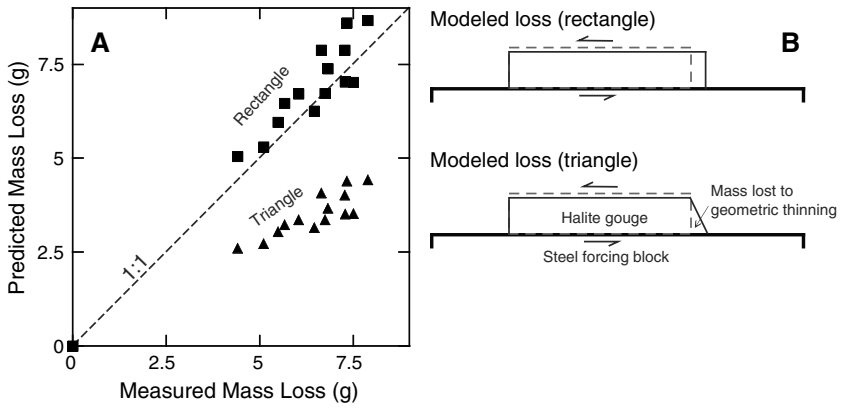

Figure 7. Mass loss occurs via geometric thinning in direct-shear experiments, which complicate porosity measurement. (b) Following *Scott et al.* [1994], we estimated mass loss with two forward models, assuming either a rectangle or triangle of material left behind. (a) We validated these models against actual material loss in 14 experiments. In general, a rectangular model best predicts mass loss for these experiments. Therefore, we used the rectangular model to estimate sample mass and porosity throughout each experiment.

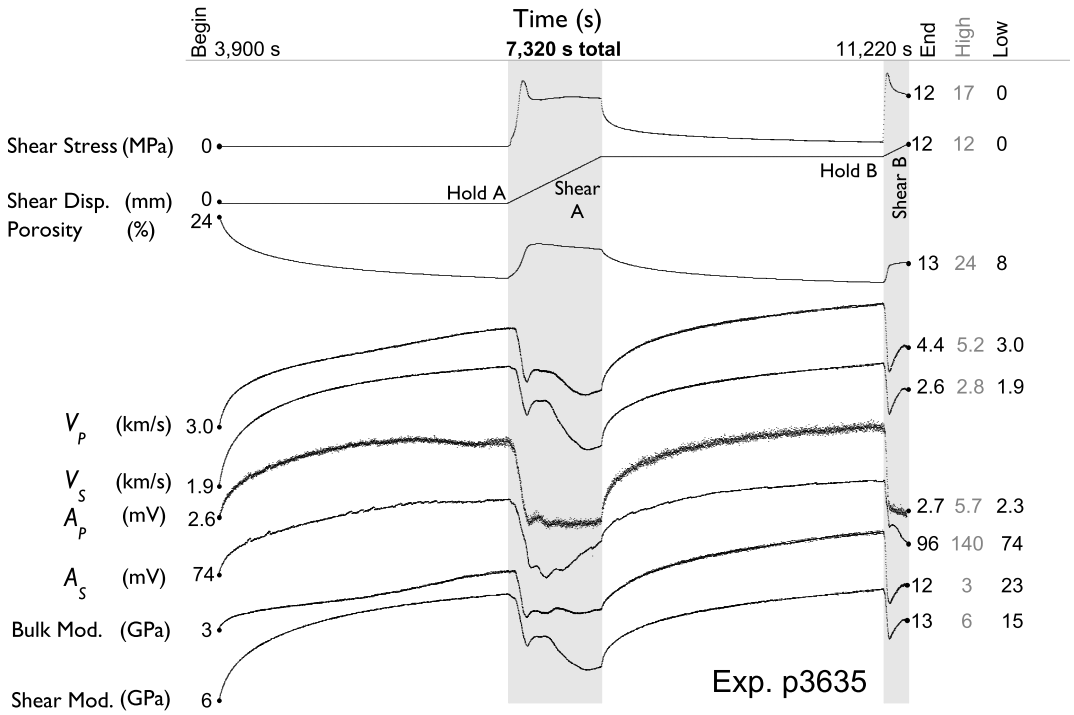

Figure 8. Details of porosity, V_P, V_S, A_P, A_S, and elastic moduli for experiment p3635. During hold periods, ϕ decreased with log(t), and the velocities, amplitudes, and moduli increased accordingly. During shear, the sample dilated and velocities and amplitudes decreased. In general, V_P, V_S, A_P, A_S, K, and G scale inversely with porosity; however, some second-order effects occur during shear. These effects tend to coincide with peak stress and peak dilatancy rate (peak $\delta\phi/\delta\gamma$).

Figure 7 shows a comparison of predicted mass lost versus the actual mass lost for the calibration experiments (Table 1) and shows that a rectangular mass loss model fits our data well. We validated the rectangular loss model by back predicting the initial sample mass and comparing it to the known initial sample mass (Table 1). The agreement is quite good (Figure 7). Therefore, we used a rectangular model to predict the sample mass and ϕ throughout our experiments (e.g., Figure 5a).

We use brine-saturated samples, and therefore, we account for the mass of salt precipitated out of the brine after the sample was dried at the end of each experiment. The actual porosity is calculated at the end of the experiment following

$$\rho_{\text{meas}} = \rho_{\text{solids}} * (1 - \phi_{\text{actual}}) + 0.32 \ \text{g/cm}^3, \tag{10}$$

where ρ_{meas} is the measured bulk density at the end of the experiment, ϕ_{actual} is the final porosity, and 0.32 g/cm^3 is the amount of salt per cubic centimeter of saturated brine.

The two primary contributors to ϕ error are layer thickness and mass measurement error. Like velocity uncertainty, these factors affect the absolute values, since they are zero points that are carried throughout each experiment. Layer thickness uncertainty was discussed in the previous section. Mass error comes from imperfect sample recovery at the end of an experiment, and we assume ±5% as a precaution. A second source of mass error comes from the geometric thinning model (Figure 7). To estimate this error, we considered a range of shape factors from 1.2 to 0.9 (1 being rectangular and 0.5 being triangular), which encompasses the data from our geometric thinning calibration. Figure 5 shows representative ϕ error for one experiment, from +11 to −3% relative to the center value.

3. Results

Our experiments began with a period of simple compaction, wherein samples were subject to normal stress (σ_n) and zero macroscopic shear stress. Under simple compaction, porosity in the laboratory fault zones dropped from ~50% to ~10% over a few hours. Figure 4 highlights ϕ evolution throughout a simple

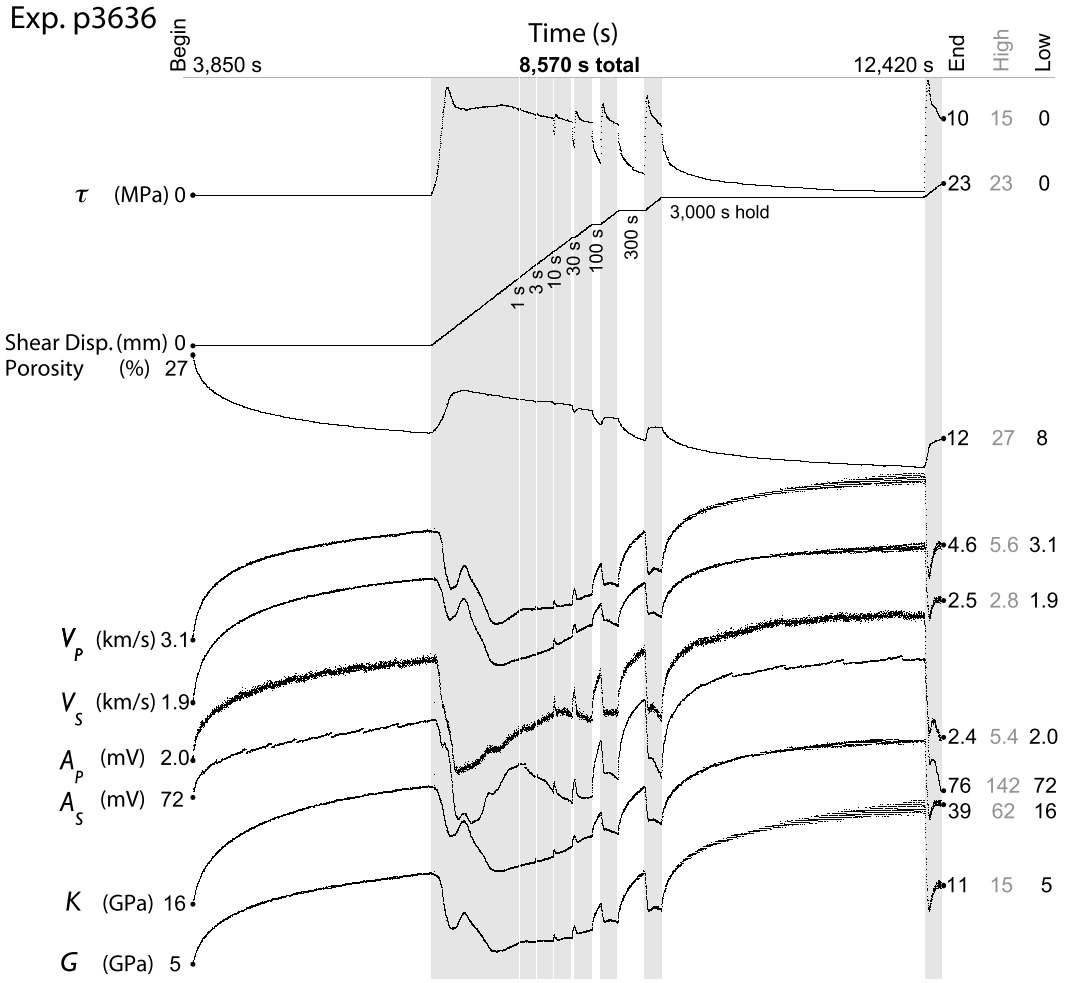

Figure 9. Detailed experiment plot over multiple shear and hold periods (1, 3, 10, 30, 100, 300, and 3000 s). Changes in ϕ, velocities, and amplitudes for initial compaction and shear were similar to p3635 (Figure 8). Across multiple hold and shear periods, the sample compacted and dilated, respectively, and hysteresis was limited (barring an overall porosity decrease over the course of the experiment). Velocities, amplitudes, and moduli generally maintained their inverse linearity with ϕ throughout the experiment.

compaction experiment (p3455). Within 4000 s at 0.5 MPa σ_n, the sample compacted from 50% to 30% porosity (Figure 4). With normal stress increased to 15 MPa, the sample underwent a second stage of compaction from 30% to 8% ϕ in ~10,000 s. Similarly, elastic wave speed and amplitude increased with compaction (Figure 4), as V_P and V_S doubled, and A_P and A_S increased tenfold.

In general, *P* and *S* waves had large amplitudes, yielding high-fidelity *P* and *S* wave arrival picks (Figure 3). Early in the experiments, however, A_P was small (0.4 mV) relative to electronic noise (±0.2 mV), affecting pick quality (Figure 4). Even these poor picks had reasonable correlation coefficients (>0.8; maximum range from −1 to 1). At higher loads, A_P increased, and the correlation coefficients became much higher (e.g., 0.95 after 15 MPa σ_n). *S* wave correlation coefficients were generally high (>0.97). This quality reflects the signal strength of A_S, generally 20X larger than A_P.

3.1. Shear Experiments

To investigate the evolution of elastic properties in fault gouge during the seismic cycle, we conducted experiments with periods of shear and nonshear (hold) as analogs for coseismic slip and interseismic quiescence. The following sections focus on two representative "slide-hold-slide" experiments: p3635 and p3636. Following initial shear, p3635 had one hold period (3000 s) followed by 2 mm of shear (Figure 8). Whereas p3636 had multiple hold periods

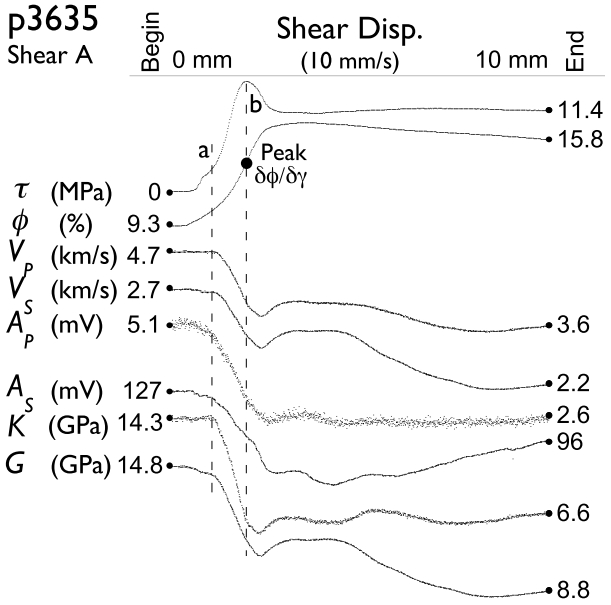

Figure 10. Changes in shear stress (τ), porosity, and elastic wave speeds and amplitudes during initial shear. With early shear (prior to point a), the sample dilated from 9% to 16% porosity and V_P, V_S, A_P, and A_S decreased. Bulk (K) and shear (G) modulus are derived from V_P, V_S, and ϕ, thus reflecting changes in those variables. Peak $\delta\phi/\delta\gamma$ coincides with peak stress [*Marone et al.*, 1990], and beyond this point, velocity and amplitude diverge from their typical trends with ϕ.

(1–3000 s), each followed by 2 mm of shear (Figure 9). During these experiments, the fault zones tended to compact during holds and dilate with fault slip.

The initial section for each experiment shows simple compaction under normal load, similar to p3455 (Figure 4). Figures 8 and 9 show the full record of loading and material response. During shear, the gouge layers tend to dilate initially, reaching a steady porosity with limited compaction (shaded portions of Figures 8 and 9). Ultrasonic velocities and amplitudes tend to inversely relate to porosity changes (Figures 8 and 9).

Figure 10 highlights the deformation that occurs during initial shear in experiment p3635 (Figure 8), along with changes to V_P, V_S, A_P, and A_S. With initial load, the sample deformed elastically, driving large τ increase. Near peak τ, the sample transitioned from elastic to inelastic deformation and the initiation of frictional shear. The sample dilated from 9% to 17% ϕ within the first 3 mm of shear. Across all experiments, dilation occurred with initial shear, peaking within the first ~2 mm of shear or ~40% shear strain. Following this period, samples tended to slowly and steadily compact with strain. During shear, the ultrasonic measurements generally reflected these porosity changes.

Elastic wave speed and amplitude show three primary phases of behavior during shear loading (Figure 10). During initial shear and dilation, V_P, V_S, A_P, and A_S generally remain constant (until point "a"; Figure 10). With the onset of rapid dilation, elastic wave speeds and amplitudes decreased to near precompaction values (from points a to "b" in Figure 10; see Figure 8). Finally, at the peak dilatancy rate (peak $\delta\phi/\delta\gamma$; point b, Figure 10) the elastic property changes flatten (Figure 10). For the remainder of the shear period following peak $\delta\phi/\delta\gamma$ (i.e., 2 to 10 mm), V_P and V_S briefly increased (2–5 mm), decreased (5–9 mm), and increased again (9–10 mm). Alternatively, A_P and A_S decreased from 2 to 4 mm and slowly increased for the remainder of shear. Similar trends occurred with initial shear during p3636 (Figure 9) and in both experiments with shear following long holds (e.g., 3000 s; Figures 8 and 9). Changes in V_P and V_S during shear are consistent with changing compaction state, grain contact quality and geometry, grain coordination number, grain contact stiffness, and grain crack density [e.g., *Khidas and Jia*, 2012; *Knuth et al.*, 2013].

Experiments with chemically assisted healing via pressure solution, such as these, tend to have very large peak stress values following holds. This reproducible peak is related to fault healing and tends to increase with log time. The healing rates from p3635 and p3636 were 0.15 $\Delta\mu$ per decade (where $\Delta\mu$ is change in friction coefficient, or $\Delta\tau/\sigma_n$), consistent with previous work [*Niemeijer et al.*, 2008].

Following initial slip, shear displacement was stopped, and the samples were held under constant normal stress, allowing compaction and creep relaxation (Figure 8). Note that these slide-hold-slide experiments do not include removal of the shear load. The reduction in shear load occurs via inelastic creep and compaction within the fault zones (Figure 8), and we observe porosity reduction with attendant changes in V_P, V_S, A_P, A_S, bulk modulus (k), and shear modulus (G; Figures 8 and 9).

The observation of dilation during shear and compaction during hold periods is robust within our suite of experiments. These trends continued regardless of the total displacement (0–23 mm) and over many

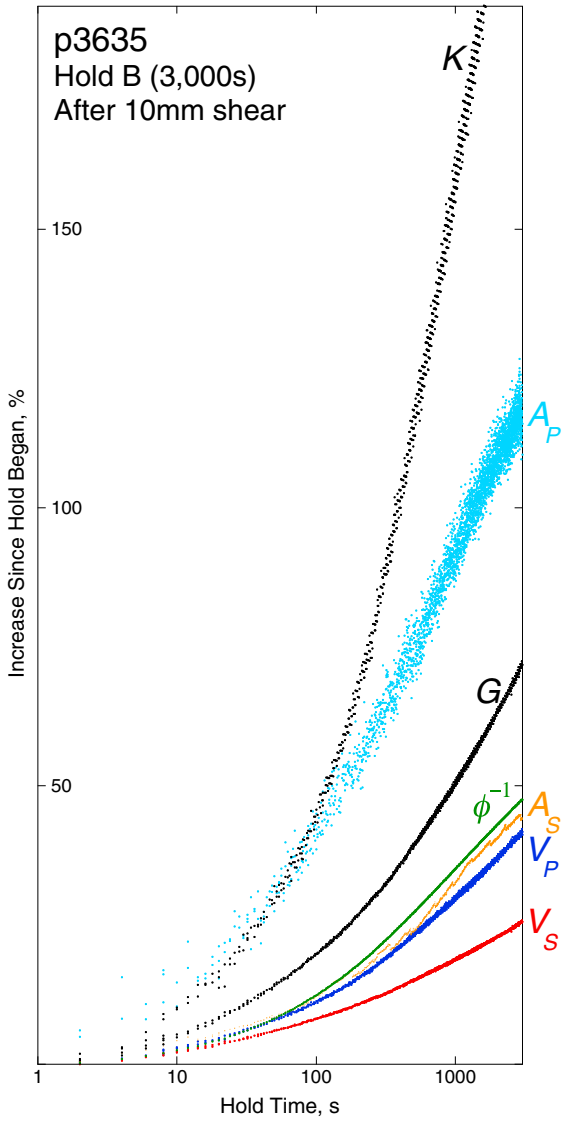

Figure 11. During holds, elastic wave speeds and amplitudes increase with log time along with ϕ decrease. A_P changes were strongest, increasing by 55% per decade. Initial changes (<~300 s) in ϕ, velocities, and amplitudes were limited, perhaps owing to a "cutoff time" for dominant pressure solution [*Niemeijer et al.*, 2008].

slide-hold-slide cycles in experiment p3636. In particular, the 3000 s holds and subsequent shear periods from p3635 (Figure 8) and p3636 (Figure 9) are quite similar.

Figure 11 highlights changes in elastic properties as a function of log time for the hold period following shear for experiment p3635. In this particular case, porosity decreased by up to 26% per decade increase in hold time (e.g., 1, 10, and 100 s). A_P was the most sensitive parameter during holds, increasing by 125% during this 3000 s hold (Figure 11), and V_S was the weakest, increasing by only 25%. Figure 12 compares these results to three other experiments (p3453, p3456, and p3457), highlighting the reproducibility of the laboratory observations. During holds following shear, τ decayed with log time, resulting from sample creep under load (e.g., Figure 8). This behavior is typical during holds in many granular materials [e.g., *Marone*, 1998; *Niemeijer et al.*, 2010; *Brantut et al.*, 2013], but the nearly complete shear stress decay over a short period of time is unique to halite (Figures 8 and 9), owing to rapid pressure solution.

3.2. Porosity-Velocity Relationships

Porosity tends to be the dominant factor controlling elastic wave speed and amplitude. Under simple compaction, these signals increase as porosity decreases (Figure 4). Under more complex loading conditions, this relationship holds during multiple compaction and dilation periods (Figure 6). We further evaluate these relationships by directly comparing V_P, V_S, A_P and A_S with ϕ for experiments p3635 and p3636 (Figures 13 and 14). Figure 13 (top row) shows a time series of porosity changes during a hold-slide-hold-slide experiment, with annotation to indicate the initial porosity (triangle), the porosity at the end of the first period of shear (circle), and the porosity at the end of the second period of shear (square). Figure 13 highlights the details of the changes for the first "hold-slide" experiment (Figure 13, left column) and the second hold-slide experiment (Figure 13, right column).

During initial compaction, V_P, V_S, A_P and A_S generally increased linearly as ϕ decreased (Figure 13). Through all of our experiments, we found that a 1% decrease in ϕ resulted in respective increases of V_P, V_S, A_P and A_S of 3%, 2%, 10%, and 7% on average. The trends of wave speed and amplitude versus porosity were similar for all of our experiments (Figure 12). Indeed, these changes even reflect the subtle change in porosity loss with log time, which occurs at a critical ϕ value from ~7 to 9% (Figure 12a).

During shear, each of the ultrasonic signals generally decreased with dilation (Figure 13, gray lines). However, these signals broke from linear trends with ϕ after the peak dilatancy rate was achieved (Figures 13 and 14). This initial shear period (0–~2 mm) accounts for a majority of the V_P, V_S, A_P and A_S decrease, and similar changes occurred following holds (Figure 13, right column). Following peak dilatancy rate, however, V_P and V_S

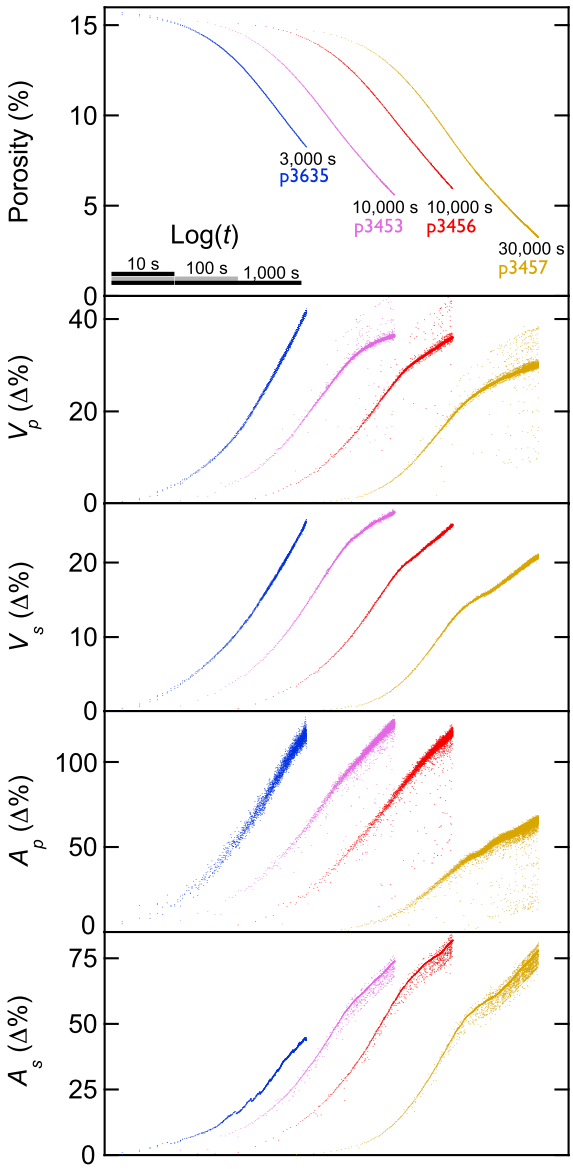

Figure 12. Porosity, velocity, and amplitude changes are consistent across these experiments, even under varied stress and strain histories (Table 1). In particular, the log linear changes in ϕ, V_P, V_S, A_P and A_S during holds are robust.

started to scale positively with ϕ. This aberrant relationship occurred in multiple experiments and is consistent with previous work [*Knuth et al.*, 2013]. Unlike sound velocities, amplitudes became more sensitive to dilation following peak $\delta\phi/\delta\gamma$ (Figures 13 and 14). These aberrant trends held until ~8 mm of shear, after which elastic wave speeds and amplitudes resumed their typical trends with bulk ϕ (Figure 13).

After short holds (i.e., <1000 s), the velocities and amplitudes decreased with dilation and showed little to no second order effects (Figure 14). In particular, the velocities experienced little hysteresis with respect to compaction during holds. The amplitudes however were more sensitive to porosity changes with dilation than compaction (Figure 14).

Through the healing periods, ϕ decreased rapidly, and the elastic wave speeds and amplitudes reflected these changes. Compaction also caused frictional strength to increase as expected for a granular materials undergoing brittle, dilatant shear [e.g., *Marone*, 1998]. Figure 15 shows that fault strength tends to increase linearly with log time (~0.15 per decade in time) and that V_P and V_S, respectively, increase by 15 and 7% per decade. Because these variables are mutually dependent on ϕ, elastic wave speed changes might be a useful tool to monitor fault strength evolution in nature. In these experiments, a 1% increase in V_P and V_S was indicative of fault strength increase by ~0.01 and ~0.02 $\Delta\mu$, respectively (Figure 15c).

4. Discussion

Our experiments replicate coseismic damage and subsequent healing within fault zones during slide-hold-slide tests. We used elastic waves to make continuous high-fidelity measurements of fault gouge evolution during these laboratory seismic cycles. During fault healing, we observe elastic wave speed increases of 20–40% and amplitude increases of 50–100%, and we observe comparable decreases with shear. These results are similar to previous laboratory results showing coseismic sound velocity decrease and log linear interseismic recovery in a dynamic system [*Kaproth and Marone*, 2013]. The velocity increases measured here far exceed velocity changes observed in the region surrounding faults in nature (e.g., ~2% V_S increase [*Li et al.*, 2006]). We believe that spatial scale is an important consideration when comparing our data to field studies, as large changes in elastic properties may be limited to the active fault zone.

We show that changes in fault zone elastic properties generally relate to compaction and dilation. During the "interseismic" periods following shear, for every 1% ϕ decrease, V_P generally increases by 3%, V_S by 2%, A_P by 10%, and A_S by 7% (Figure 11). During shear, we observe large changes in elastic wave speed and amplitude, with initial decreases occurring during dilation followed by more subtle velocity changes during steady frictional shear. This

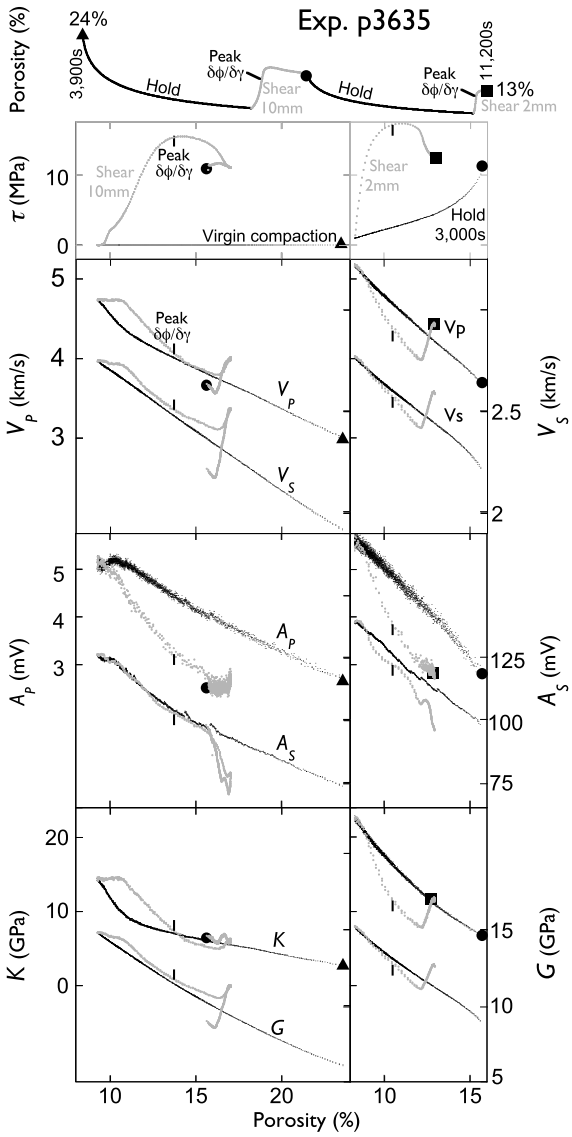

Figure 13. Elastic wave speeds and amplitudes with porosity for an experiment with two shear periods. The initial hold and shear period are shown in the left column, with the subsequent hold and shear in the right column. V_P, V_S, A_P, and A_S tend to scale linearly with inverse porosity, and this relation is strongest during compaction (black). With shear (gray), V_P and V_S generally decrease with dilation, but these trends break down following peak $\delta\phi/\delta\gamma$: V_P and V_S develop a positive linear relationship with ϕ, and A_P and A_S become more sensitive to ϕ change. Velocities and amplitudes appear to revert to their original trends with ϕ near the end of the first shear period (green dot).

finding indicates that while elastic wave speed may be useful for estimating interseismic fault healing, it may not be a reliable indicator of cumulative coseismic fault displacement.

4.1. The Role of Compaction

Healing during our experiments occurred via pressure solution, which is applicable in nature over long time scales and in chemically active environments [*Bos and Spiers*, 2000; *Niemeijer et al*., 2008]. Our experiments follow the work by *Niemeijer et al*. [2008] and show three lines of evidence for pressure solution: (1) linear stress relaxation with log time during holds, with near-complete stress relaxation; (2) high rates of frictional healing (up to 0.15 $\Delta\mu$ per decade); and (3) porosity loss to $<$10%, well below nonchemical compaction limits for granular materials.

Pressure solution, fault healing, and brecciation may occur cyclically during the seismic cycle in nature and in these experiments [e.g., *Sleep and Blanpied*, 1992]. We observe bulk compaction with σ_n increase (0.5 to 15 MPa; Figure 4) and following shear (Figure 2). Pressure solution is favored with increased load, as stress changes alter the NaCl concentration gradient, prompting further erosion at grain contacts. Pressure solution occurs following shear, as dilation likely disrupts the old framework of load-supporting grain necks, replacing them with new, sharp grain contacts that are prone to rapid pressure solution.

Porosity loss with pressure solution is expected to cause significant changes in the elastic wave speeds and amplitudes. Previous works show that elastic velocities generally increase linearly with ϕ loss [*Hadley*, 1976; *Popp and Kern*, 1998; *Schubnel et al*., 2003; *Fortin et al*., 2005, 2007; *Croizé et al*., 2010], and our results corroborate these findings. Moreover, we see that V_P and V_S for our dense granular fault zones approach the velocities for crystalline halite [*Popp and Kern*, 1998; *Mavko et al*., 2009]. The relationship between ϕ and elastic wave speed is driven by increased interparticle contact stiffness, grain coordination number, and intragranular crack healing, which increase the bulk and shear moduli [*Digby*, 1981; *Makse et al*., 2004; *Mavko*, 2009; *Khidas and Jia*, 2010, 2012; *Knuth et al*., 2013]. Amplitude changes occur along with velocity, driven by reduced density contrast [*Stein and Wysession*, 2003] between the experimental fault zones and the forcing blocks, which act as wall rock.

4.2. The Role of Shear

Similar to the compaction period, porosity relates strongly with elastic wave speed and amplitude during fault slip and dilation (Figures 4, 6, 8, and 9). With early shear (0 to ~2 mm), the fault layer dilates (e.g., from 9

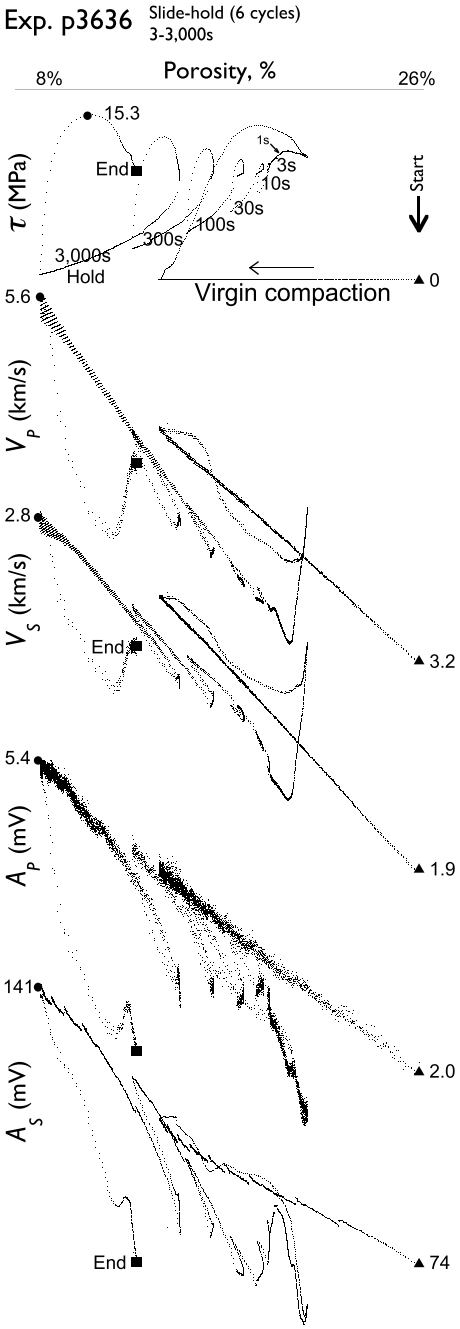

Figure 14. Elastic wave speeds and amplitudes with porosity for a multiple hold-and-shear period experiment. Velocities and amplitudes scale with inverse porosity over multiple-shear periods, driving dilation, and compaction periods during holds (1–3000 s). Like p3635 (Figure 13), typical trends break down during the initial shear period and similarly revert to original trends near the end of this shear interval. Similar behavior also occurs with shear following the 3000 s hold. Alternatively, V_P, V_S, A_P, and A_S maintain their inverse linearity with ϕ following short holds. We suggest that fabric developed during initial shear remains active after short holds and that healing during long holds makes new fabric networks preferable.

to 17% ϕ; Figure 10). Dilation is a well-established granular response to shear [*Mead*, 1925; *Marone et al.*, 1990]. During initial shear, the stress field orients away from σ_n and the wave propagation direction, potentially affecting contact geometries and the elastic wave speeds [*Khidas and Jia*, 2012; *Knuth et al.*, 2013]. The inverse linear relationship between elastic wave speeds and amplitudes with ϕ is most consistent following short holds (i.e., $<$1000 s; Figure 13). These expected trends break down however during initial shear or after long holds (Figures 13 and 14). In the following section, we examine the potential effect of fabric formation on elastic wave speeds and amplitudes, and we consider the utility of ultrasound as a probe for fault fabric development.

4.3. The Run-In: From Distributed to Localized Shear

As shear stress is applied to a fault zone of finite width, granular shear begins almost immediately and drives dilatation (e.g., from points a to b, Figure 10). This ϕ increase, along with principal stress rotation, results in elastic wave speed and amplitude decrease. During this initial period, the dilatancy rate continually ($\delta\phi/\delta\gamma$) increases. As the dilatancy rate begins to decrease, which coincides with the peak in shear strength (Figure 10), the macroscopic dilation of the fault zone ceases and gives way to constant porosity or slight dilation or compaction. Changes in trends between V_P, V_S, A_P, and A_S with ϕ are coincident with peak stress and peak dilatancy rate (Figures 10, 13, and 14) and may be caused by a transition from localized to distributed deformation [*Frank*, 1965; *Logan et al.*, 1979; *Marone and Scholz*, 1989; *Marone et al.*, 1990]. Peak frictional strength, maximum dilatancy rate, and the change in gouge deformation style are interrelated and can be understood in terms of energetics.

Dilation requires work against normal stress and results in higher shear strength. It is clear that dilatancy rate is directly tied to frictional strength from the relation:

$$\tau = \tau_f + \sigma'_n * \delta\phi/\delta\gamma, \quad (11)$$

where τ_f is the frictional resistance and σ_n' is the effective normal stress [*Marone et al.*, 1990]. We observe that prior to peak $\delta\phi/\delta\gamma$, the rate of dilation increases with strain, and thus, the energy required for shear increases with strain, driving distributed deformation. For example, a "localized" zone during this period has higher strain, incrementally requiring more energy [*Frank*, 1965]. Alternatively, neighboring less strained zones require less energy and are thus preferred for shear, resulting in distributed deformation. Following peak $\delta\phi/\delta\gamma$, however, dilatancy rate decreases with strain, requiring less energy for shear and promoting localization. Previous works show that localized zones (i.e., Riedel shears) tend to initiate near peak $\delta\phi/\delta\gamma$ [*Marone and Scholz*, 1989; *Marone et al.*, 1990; *Haines et al.*, 2013]. Figure 16 is a thin section

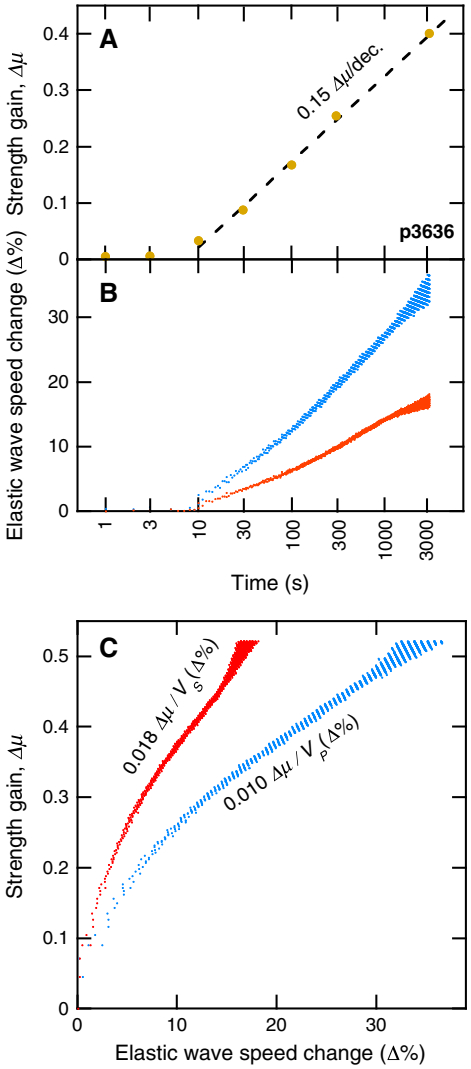

Figure 15. (a) Fault strength and (b) elastic wave speeds increase with log time during holds. Elastic wave speed changes correspond to porosity change. Strength increase also depends on porosity change, as shear will require greater work against normal stress. Elastic wave speeds may thus be a useful proxy for in situ fault strength changes, since both are dependent on porosity. (c) In these experiments, strength increases by ~0.01 and ~0.02 $\Delta\mu$ per percent increase of V_P and V_S.

scanning electron micrograph (SEM) from sample p3620, showing well-developed networks of Riedel shears with some boundary parallel *Y* shears [e.g., *Niemeijer et al.*, 2010]. We note that in situ porosity is much lower than the porosity following sample removal and drying, which results in fabric opening.

4.4. The Role of Fabric Development

After peak $\delta\phi/\delta\gamma$, the elastic wave speeds and amplitudes diverge from linearity with inverse porosity (Figures 13 and 14). V_P and V_S transition to a positive relationship with ϕ, contradicting expected trends [e.g., *Nur et al.*, 1998; *Popp and Kern*, 1998]. Some previous experimental works have identified similar trends due to intergranular cracking [*Fortin et al.*, 2007] and force chain development [*Khidas and Jia*, 2012; *Knuth et al.*, 2013], but neither of these mechanisms can account for the disparate trends of velocities and amplitude with ϕ. Instead, fabric generation following peak $\delta\phi/\delta\gamma$ may provide the most viable explanation for this disparity.

Within a fault, localized shear zones accommodate most strain once they being to form [*Logan et al.*, 1992; *Rathbun and Marone*, 2010; *Haines et al.*, 2013]. The three dominant types of fabric are R1 (Riedel shear), R2, and *Y* shear zones, and they occur over a wide range of materials and conditions. Similar to our observations (e.g., Figure 16), *Niemeijer et al.* [2010] documented Riedel shears at low shear strains with halite (~2.5 γ). These tend to occur at high angles to σ_n, subparallel to the sound wave propagation direction in our experiments.

Riedel shears may confound our ultrasonic measurements, which are sensitive to local heterogeneities, but these anomalies may provide information about Riedel shear formation. In general, V_P and V_S represent the fastest *P* and *S* waves to propagate through the fault layers and forcing blocks. In a case with distributed deformation, all direct travel paths between the PZTs are equally fast. Alternatively, with localized deformation, certain pathways become preferentially faster. The localized shear zones are likely slow, owing to increased porosity driven by shear and increased intergranular cracking [*Fortin et al.*, 2007]. In contrast, the nonlocalizing regions can flow back to their original state [*Khidas and Jia*, 2012] and may undergo pressure solution and compaction. Therefore, V_P and V_S likely represent velocity changes along specific, fast pathways, whereas the ϕ measurements represent changes to the bulk sample. This skews the apparent relationships between the velocities and ϕ.

In contrast to elastic wave speeds, amplitudes become more sensitive to ϕ following peak $\delta\phi/\delta\gamma$ (Figures 13 and 14), but may also be understood in terms of fabric development. In the homogeneous case, *P* waves arrive *en masse* and make an impulsive amplitude signal. However, with slow (shear zones) and fast (spectator regions) pathways created by fault fabric, dispersion occurs, and the *P* waves arrive at slightly different times, blurring the signal. This *energy splitting* should similarly occur for *S* waves. Thus, wave velocities and amplitudes may not be primarily controlled by the bulk porosity but, respectively, by the porosity of the fastest travel paths and energy splitting.

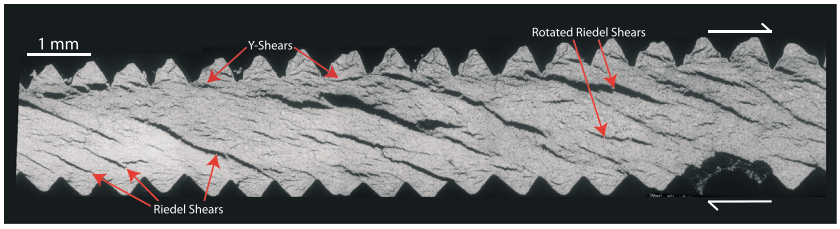

Figure 16. Thin-section SEM from experiment p3620 ($\gamma = 4.6$). The fault zone developed pervasive and throughgoing Riedel shear networks typical of granular materials [e.g., *Logan et al.*, 1992; *Niemeijer et al.*, 2010; *Haines et al.*, 2013]. Riedel shears tend to rotate with shear strain [*Haines et al.*, 2013] and may become subparallel to the shear direction (perpendicular to *P* and *S* wave propagation). Boundary-parallel *Y* shears are also evident and occur at the interface with the steel forcing block teeth.

Near peak dilation, as opposed to peak $\delta\phi/\delta\gamma$, elastic wave speeds decrease, and amplitudes increase and maintain their anomalous trends with ϕ (Figures 13 and 14). These changes may be understood by considering fabric evolution, as Riedel shears tend to rotate from high to low angles from σ_n with shear [*Logan et al.*, 1992; *Haines et al.*, 2013]. For example, Figure 16 shows rotated Riedel shears, which occur subparallel to the shear direction. With Riedel rotation, the fastest velocity travel paths become longer and must eventually cross these zones, driving velocity decrease. As the fastest waves become slower, their arrival becomes closer to the slowest waves, limiting energy splitting and increasing amplitude. While fabric rotation explains the velocity increase followed by decrease, it does not offer an explanation for the apparent positive linear relationship that develops with ϕ (Figures 13 and 14), a trend that appears to hold through the periods of bulk dilation and compaction. Whether this trend is coincidental or consequential remains an open question.

At the end of the run-in (e.g., shear displacement of 8–10 mm; Figure 10), velocities and amplitudes reassume their inverse linear trends with porosity (Figures 13 and 14). At high strains, fabric may rotate subperpendicular to σ_n [*Haines et al.*, 2013] and the wave propagation direction, diminishing preferred travel paths for sound waves. In this case sound waves must travel across heterogeneous zones. Therefore, any changes to bulk porosity are experienced by all waves, and the expected trends of velocities and amplitudes with ϕ are resumed.

We posit that high-frequency ultrasonic measurements are sensitive to fabric generation in fault zones at the laboratory scale. The apparent development of steady state fabric during these experiments further supports the idea of using a laboratory *run-in*, as a proxy for developing a mature fault zone and to ensure experimental reproducibility [*Shimamoto and Logan*, 1981; *Marone*, 1998].

4.5. Velocity Evolution During Shear: The Coseismic Analog

We find that the relationship between porosity and ultrasonic signals is strong over short holds (1–300 s) and the following shear periods (Figure 14). This is different from the run-in period, where velocity-porosity relationships break down during shear. This behavior indicates that the steady state fabric established during the run-in persists and remains active with further shear, similar to the observations of *Khidas and Jia* [2012].

In contrast, following long holds, the elastic wave speeds and amplitudes exhibit behavior that is similar to the run-in. With initial shear following long holds (e.g., 3000 s), V_P, V_S, A_P and A_S decrease with dilation, followed by a period of increasing velocities, and stronger amplitude decreases with further dilation (Figures 13 and 14). This behavior indicates a new period of fabric formation, perhaps necessitated by welding between grains resulting from pressure solution.

5. Conclusions and Implications for Natural Fault Zones

These experiments provide detailed observations of fault zone damage during fault slip and subsequent fault healing. Our elastic wave speed observations show behaviors similar to previous works near natural fault zones, including coseismic velocity decrease followed by recovery with log time. However, we observe much larger signals overall. Previous works in nature generally focus on regional velocity changes, which likely result from dewatering, fracture, crack opening, and regional stress changes. To date, fault zone guided

waves provide the highest-resolution observations around faults, ~200 m [e.g., *Li et al*., 2003, 2006], but these are wide relative to the active fault zone during dynamic shear, which may be quite narrower [*Faulkner et al*., 2010; *Di Toro et al*., 2011]. Our observations monitor the fault zone itself, and we observe very large elastic wave speed and amplitude changes. These changes are driven by dilation and fabric formation during shear and compaction via pressure solution during interseismic periods.

Porosity is the dominant control on elastic wave speeds and amplitudes throughout our experiments. Per 1% ϕ loss, V_P generally increases by 3%, V_S by 2%, A_P by 10%, and A_S by 7% (Figure 11), and these trends tend to persist with shear-induced dilation (Figure 6). Through the healing periods, ϕ generally decreases by ~25% per decade (Δ%) and occurs in tandem with strength increase (~0.15 $\Delta\mu$ per decade). This work indicates that changes to V_P and V_S through interseismic periods may be a useful tool to measure fault strength changes. Figure 15 shows that for a 1% change in V_P and V_S, frictional strength might, respectively, increase by ~0.01 and ~0.02. Similar experiments could be used to catalog strength proxy observations for other fault zone materials. To estimate bulk porosity and thus fault strength evolution in nature, acoustic measurements must be made through a fault zone, perhaps using fault zone trapped waves or with borehole observatories similar to SAFOD [e.g., *Li et al*., 1998; *Niu et al*., 2008].

Our experiments may provide insight on velocity evolution during fault rupture, highlighting the potential importance of fault dilation and fabric formation for elastic wave speeds and amplitudes. Our observations were limited to quasistatic slip and thus lack some coseismic processes; however, coseismic deformation is difficult to observe in detail due to the high slip velocities, small risetimes, and noise from seismic energy. Our results suggest that V_P and V_S changes do not scale with total fault slip, since most damage occurs with early shear, and should not be used as an indicator for earthquake magnitude. However, this may not be the case for observations of velocity decrease in earthquake damage zones. In damage zones, velocity loss is more likely related to brecciation and damage accumulation and may be closely related to earthquake magnitude [e.g., *Brenguier et al*., 2008; *Li et al*., 2003, *Rubinstein and Beroza*, 2005; *Nakata and Snieder*, 2011].

Our results suggest that ultrasonic velocities and amplitudes may provide a proxy to monitor fabric formation within laboratory fault zones. Although fabric also occurs in nature, these fine structures may be obscured using lower frequency sound waves, making them difficult or impossible to observe in the field. While porosity changes are the main control on elastic wave speeds and amplitudes, fabric formation can dominate this signal and influence expected velocity-porosity relationships. During fabric formation, the fault gouge develops heterogeneities. These localized zones cause sound waves to follow preferred travel paths, which result in velocity increase and amplitude decrease as these zones develop. The observations of subsequent velocity decrease and amplitude increase highlight Riedel rotation to near perpendicular with σ_n. At high strains, the elastic wave speeds and amplitudes resume expected trends with ϕ, indicating that steady state fabric has been developed and validating the efficacy of run-in periods for friction experiments. We observe fabric formation during the run-in and after long holds, and similar processes likely occur in young faults and in faults with chemically assisted healing.

Acknowledgments

We thank all the members of the Penn State Rock and Sediment Mechanics Laboratory, past and present, for their support and guidance. We give special thanks to Matt Knuth, who helped develop our ultrasonic measurement capabilities; Steve Swavely for his excellent technical assistance; and Chuck Ammon for his guidance with elastic wave speed interpretations. We gratefully acknowledge support from the National Science Foundation: OCE-0648331, EAR-0746192, and EAR-0950517. All data are stored in the Penn State Rock and Sediment Mechanics Laboratory data repository and will be made available upon request.

References

Anthony, J. L., and C. Marone (2005), Influence of particle characteristics on granular friction, *J. Geophys. Res.*, *110*, B08409, doi:10.1029/2004JB003399.

Baisch, S., and G. H. R. Bokelmann (2001), Seismic waveform attributes before and after the Loma Prieta earthquake - Scattering change near the earthquake and temporal recovery, *J. Geophys. Res.*, *106*(B8), 16,323–16,337, doi:10.1029/2001JB000151.

Bos, B., and C. J. Spiers (2000), Effect of phyllosilicates on fluid-assisted healing of gouge-bearing faults, *Earth Planet. Sci. Lett.*, *184*(1), 199–210.

Brace, W., and J. Byerlee (1966), Stick-slip as a mechanism for earthquakes, *Science*, *153*, 990–992.

Brantut, N., M. J. Heap, P. G. Meredith, and P. Baud (2013), Time-dependent cracking and brittle creep in crustal rocks: A review, *J. Struct. Geol.*, *52*, 17–43.

Brenguier, F., M. Campillo, C. Hadziioannou, N. M. Shapiro, R. M. Nadeau, and E. Larose (2008), Postseismic relaxation along the San Andreas Fault at Parkfield from continuous seismological observations, *Science*, *321*, 1478–1481.

Chao, K., and Z. Peng (2009), Temporal changes of seismic velocity and anisotropy in the shallow crust induced by the 1999 October 22 M6. 4 Chia-Yi, Taiwan earthquake, *Geophys. J. Int.*, *179*, 1800–1816.

Croizé, D., K. Bjørlykke, J. Jahren, and F. Renard (2010), Experimental mechanical and chemical compaction of carbonate sand, *J. Geophys. Res.*, *115*, B11204, doi:10.1029/2010JB007697.

Di Toro, G., R. Han, T. Hirose, N. De Paola, S. Nielsen, K. Mizoguchi, F. Ferri, M. Cocco, and T. Shimamoto (2011), Fault lubrication during earthquakes, *Nature*, *462*, 907–910, doi:10.1038/nature09838.

Digby, P. J. (1981), The effective elastic moduli of porous granular rocks, *J. Appl. Mech.*, *48*, 803–808.

Elkhoury, J. E., E. E. Brodsky, and D. C. Agnew (2006), Seismic waves increase permeability, *Nature*, *441*(7097), 1135–8, doi:10.1038/nature04798.

Erickson, N., and R. D. Jarrard (1998), Velocity-porosity relationships for water-saturated sediments, *J. Geophys. Res.*, *103*(B12).

Faulkner, D. R., C. A. L. Jackson, R. J. Lunn, R. W. Schlische, Z. K. Shipton, C. A. J. Wibberley, and M. O. Withjack (2010), A review of recent developments concerning the structure, mechanics and fluid flow properties of fault zones, *J. Struct. Geol.*, *32*(11), 1557–1575.

Fortin, J., Y. Guéguen, and A. Schubnel (2007), Effects of pore collapse and grain crushing on ultrasonic velocities and V_P/V_S, *J. Geophys. Res.*, *112*, B08207, doi:10.1029/2005JB004005.

Fortin, J., A. Schubnel, and Y. Guéguen (2005), Elastic wave velocities and permeability evolution during compaction of Bleurswiller sandstone, *Int. J. Rock Mech. Min. Sci.*, *42*(7–8), 873–889.

Frank, F. C. (1965), On dilatancy in relation to seismic sources, *Rev. Geophys.*, *3*(4), 485–503, doi:10.1029/RG003i004p00485.

Hadley, K. (1976), Comparison of calculated and observed crack densities and seismic velocities in westerly granite, *J. Geophys. Res.*, *81*(20), 3484–3494, doi:10.1029/JB081i020p03484.

Haines, S., B. Kaproth, C. Marone, D. Saffer, and B. van der Pluijm (2013), Shear zones in clay-rich fault gouge: A laboratory study of fabric development and evolution, *J. Struct. Geol.*, *51*, 206–225.

Johnson, P. A., B. Carpenter, M. Knuth, B. M. Kaproth, P.-Y. Le Bas, E. G. Daub, and C. Marone (2012), Nonlinear dynamical triggering of slow slip on simulated earthquake faults with implications to Earth, *J. Geophys. Res.*, *117*, B04310, doi:10.1029/2011JB008594.

Kaproth, B. M., S. M. Cashman, and C. Marone (2010), Deformation band formation and strength evolution in unlithified sand: The role of grain breakage, *J. Geophys. Res.*, *115*, B12103, doi:10.1029/2010JB007406.

Kaproth, B. M., and C. Marone (2013), Slow earthquakes, preseismic velocity changes, and the origin of slow frictional stick-slip, *Science*, *341*(6151), 1229–1232, doi:10.1126/science.1239577.

Khidas, Y., and X. Jia (2010), Anisotropic nonlinear elasticity in a spherical-bead pack: Influence of the fabric anisotropy, *Phys. Rev.*, *81*(2), 021303.

Khidas, Y., and X. Jia (2012), Probing the shear-band formation in granular media with sound waves, *Phys. Rev.*, *85*, 051302.

Kitajima, H., and D. M. Saffer (2012), Elevated pore pressure and anomalously low stress in regions of low frequency earthquakes along the Nankai Trough subduction megathrust, *Geophys. Res. Lett.*, *39*, L23301, doi:10.1029/2012GL053793.

Knuth, M. W., H. J. Tobin, and C. Marone (2013), Evolution of ultrasonic velocity and dynamic elastic moduli with shear strain in granular layers, *Granular Matter*, *15*, 499–515, doi:10.1007/s10035-013-0420-1.

Lazarus, D. (1949), The variation of the adiabatic elastic constants of KCl, NaCl, CuZn, Cu, and Al with pressure to 10,000 bars, *Phys. Rev.*, *76*(4).

Li, Y. G., and J. E. Vidale (2001), Healing of the shallow fault zone from 1994-1998 after the 1992 Ml. S Landers, California, earthquake, *Geophys. Res. Lett.*, *28*(15), 2999–3002, doi:10.1029/2001GL012922.

Li, Y. G., J. E. Vidale, K. Aki, F. Xu, and T. Burdette (1998), Evidence of shallow fault zone strengthening after the 1992 M7.5 Landers, California, earthquake, *Science*, *279*, 217-219, doi:10.1126/science.279.5348.217.

Li, Y. G., J. E. Vidale, S. M. Day, D. S. Oglesby, and E. Cochran (2003), Postseismic fault healing on the rupture zone of the 1999 M 7.1 Hector Mine, California, earthquake, *Bull. Seismol. Soc. Am.*, *93*(2), 854–869.

Li, Y.-G., P. Chen, E. Cochran, J. E. Vidale, and T. Burdette (2006), Seismic evidence for rock damage and healing on the San Andreas fault associated with the 2004 M 6.0 Parkfield earthquake, *Bull. Seismol. Soc. Am.*, *96*(4), S349–S363, doi:10.1785/0120050803.

Liu, Z., J. Huang, Z. Peng, and J. Su (2013), Seismic velocity changes in the epicentral region of the 2008 Wenchuan earthquake measured from three-component ambient noise correlation techniques, *Geophys. Res. Lett.*, *41*, 37–42, doi:10.1002/2013GL058682.

Logan, J. M., M. Friedman, N. Higgs, C. Dengo, and T. Shimamoto (1979), Experimental studies of simulated fault gouges and their application to studies of natural fault zones, in *Analysis of Actual Fault zones in Bedrock*, U.S. Geol. Surv. Open file Rep., 79-1239, edited by R. C. Speed and R. V. Sharp, pp. 305–343.

Logan, J. M., C. Dengo, N. Higgs, and Z.-Z. Wang (1992), Fabrics of experimental fault zones: Their development and relationship to mechanical behavior, in *Fault Mechanics and Transport Properties of Rocks*, pp. 33–67, Academic Press, San Diego, Calif.

Makse, H. A., N. Gland, D. L. Johnson, and L. Schwartz (2004), Granular packings: Nonlinear elasticity, sound propagation, and collective relaxation dynamics, *Phys. Rev. E*, *70*, 061302.

Marone, C., and C. H. Scholz (1989), Particle-size distribution and microstructures within simulated fault gouge, *J. Struct. Geol.*, *11*(7), 799–814.

Marone, C., C. B. Raleigh, and C. H. Scholz (1990), Frictional behavior and constitutive modeling of simulated fault gouge, *J. Geophys. Res.*, *95*(B5), 7007–7025, doi:10.1029/JB095iB05p07007.

Marone, C. (1998), Laboratory-derived friction laws and their application to seismic faulting, *Annu. Rev. Earth Planet. Sci.*, *26*(1), 643–696.

Mavko, G., T. Mukerji, and J. Dvorkin (2009), *The Rock Physics Handbook: Tools for Seismic Analysis of Porous Media*, 2nd ed., Cambridge Univ. Press, Cambridge, U. K.

Mead, W. (1925), The geologic role of dilatancy, *Geology*, *33*(7), 685–698.

Minato, S., T. Tsuji, S. Ohmi, and T. Matsuoka (2012), Monitoring seismic velocity change caused by the 2011 Tohoku-oki earthquake using ambient noise records, *Geophys. Res. Lett.*, *39*, L09309, doi:10.1029/2012GL051405.

Nakata, N., and R. Snieder (2011), Near-surface weakening in Japan after the 2011 Tohoku-Oki earthquake, *Geophys. Res. Lett.*, *38*, L17302, doi:10.1029/2011GL048800.

Nakata, N., and R. Snieder (2012), Time-lapse change in anisotropy in Japan's near surface after the 2011 Tohoku-Oki earthquake, *Geophys. Res. Lett.*, *39*, L11313, doi:10.1029/2012GL051979.

Niemeijer, A., C. Marone, and D. Elsworth (2010), Frictional strength and strain weakening in simulated fault gouge: Competition between geometrical weakening and chemical strengthening, *J. Geophys. Res.*, *115*, B10207, doi:10.1029/2009JB000838.

Niemeijer, A., C. Marone, and D. Elsworth (2008), Healing of simulated fault gouges aided by pressure solution: Results from rock analogue experiments, *J. Geophys. Res.*, *113*, B04204, doi:10.1029/2007JB005376.

Niu, F., P. G. Silver, T. M. Daley, X. Cheng, and E. L. Majer (2008), Preseismic velocit changes observed for active source monitoring at the Parkfield SAFOD drill site, *Nature*, *454*, 204–208.

Nur, A., G. Mavko, J. Dvorkin, and D. Galmudi (1998), Critical porosity: A key to relating physical properties to porosity in rocks, *Lead. Edge*, *17*(3), 357–362.

Popp, T., and H. Kern (1998), Ultrasonic wave velocities, gas permeability and porosity in natural and granular rock salt, *Phys. Chem. Earth*, *23*(3), 373–378.

Poupinet, G., W. L. Ellsworth, and J. Frechet (1984), Monitoring velocity variations in the crust using earthquake doublets: An application to the Calaveras Fault, California, *J. Geophys. Res.*, *89*(NB7), 5719–5731, doi:10.1029/JB089iB07p05719.

Rathbun, A. P., and C. Marone (2010), Effect of strain localization on frictional behavior of sheared granular materials, *J. Geophys. Res.*, *115*, B01204, doi:10.1029/2009JB006466.

Rubinstein, J. L., and G. C. Beroza (2005), Depth constraints on nonlinear strong ground motion from the 2004 Parkfield earthquake, *Geophys. Res. Lett.*, *32*, L14313, doi:10.1029/2005GL023189.

Rubinstein, J. L., and G. C. Beroza (2004), Nonlinear strong ground motion in the M-L 5.4 Chittenden earthquake: Evidence that preexisting damage increases susceptibility to further damage, *Geophys. Res. Lett.*, *31*, L23614, doi:10.1029/2004GL021357.

Sawazaki, K., H. Sato, H. Nakahara, and T. Nishimura (2009), Time-Lapse Changes of Seismic Velocity in the Shallow Ground Caused by Strong Ground Motion Shock of the 2000 Western-Tottori Earthquake, Japan, as Revealed from Coda Deconvolution Analysis, *Bull. Seismol. Soc. Am.*, *99*(1), 352–366, doi:10.1785/0120080058.

Schaff, D. P., and G. C. Beroza (2004), Coseismic and postseismic velocity changes measured by repeating earthquakes, *J. Geophys. Res.*, *109*, B10302, doi:10.1029/2004JB003011.

Schaff, D. P. (2012), Placing an upper bound on preseismic velocity changes measured by ambient noise monitoring for the 2004 Mw 6.0 Parkfield earthquake (California), *Bull. Seismol. Soc. Am.*, *104*(4), 1400–1416, doi:10.1785/0120110342.

Scholz, C. (2002), *The Mechanics of Earthquakes and Faulting*, 2nd ed., pp. 81-97, Cambridge Univ. Press, Cambridge, U. K.

Schubnel, A., O. Nishizawa, K. Masuda, X. J. Lei, Z. Xue, and Y. Guéguen (2003), Velocity measurements and crack density determination during wet triaxial experiments on Oshima and Toki granites, *Pure Appl. Geophys.*, *160*, 869–887.

Scott, D. R., C. J. Marone, and G. C. Sammis (1994), The apparent friction of granular fault gauge in sheared layers, *J. Geophys. Res.*, *99*(B4), 7231–7231, doi:10.1029/93JB03361.

Shimamoto, T., and J. M. Logan (1981), Effects of simulated fault gouge on the sliding behavior of Tennessee sandstone: Nonclay gouges, *J. Geophys. Res.*, *86*, 2902–2914, doi:10.1029/JB086iB04p02902.

Silver, P. G., T. M. Daley, F. Niu, and E. L. Majer (2007), Active source monitoring of cross-well seismic travel time for stress-induced changes, *BSSA*, *97*(1B), 281–293.

Sleep, N. H., and M. L. Blanpied (1992), Creep, compaction and the weak rheology of major faults, *Nature*, *359*, 687–692.

Stein, S., and M. Wysession (2003), *An Introduction to Seismology, Earthquakes, and Earth Structure*, 1st ed., Blackwell Publishing, Malden, Mass.

Takagi, R., T. Okada, H. Nakahara, N. Umino, and A. Hasegawa (2012), Coseismic velocity change in and around the focal region of the 2008 Iwate-Miyagi Nairiku earthquake, *J. Geophys. Res.*, *117*, B06315, doi:10.1029/2012JB009252.

Vidale, J. E., and Y. G. Li (2003), Damage to the shallow Landers fault from the nearby Hector Mine earthquake, *Nature*, *421*, 524–526.

Wegler, U., and C. Sens-Schoenfelder (2007), Fault zone monitoring with passive image interferometry, *Geophys. J. Int.*, *168*(3), 1029–1033, doi:10.1111/j.1365-246C.2006.03284.x.

Xue, L. H., et al. (2013), Continuous permeability measurements record healing inside the Wenchuan earthquake fault zone, *Science*, *340*, 1555–1559.

Yamada, M., J. Mori, and S. Ohmi (2010), Temporal changes of subsurface velocities during strong shaking as seen from seismic interferometry, *J. Geophys. Res.*, *115*, B03302, doi:10.1029/2009JB006567.